CHEMISTRY OF MATERIALS

pubs.acs.org/cm

Article

Ultralow Lattice Thermal Conductivity in Metastable Ag_2GeS_3 Revealed by a Combined Experimental and Theoretical Study

Callista M. Skaggs,[▽] Andrew P. Justl,[▽] Ankita Biswas, Peter E. Siegfried, Shunshun Liu, Saul H. Lapidus, Wenqian Xu, Zachary T. Messegee, Nirmal J. Ghimire, Prasanna V. Balachandran,* Susan M. Kauzlarich,* and Xiaoyan Tan*

Cite This: *Chem. Mater.* 2022, 34, 6420−6430

Read Online

ACCESS | Metrics & More | Article Recommendations | Supporting Information

ABSTRACT: A metastable polycrystalline Ag_2GeS_3 compound was prepared at 1000 °C with binary Ag_2S and GeS_2 as starting materials. At room temperature, Ag_2GeS_3 was determined to adopt a polar orthorhombic crystal structure (space group $Cmc2_1$) based on the Rietveld refinement of synchrotron X-ray diffraction data. The crystal structure consists of layers of distorted AgS_4 and GeS_4 tetrahedra stacked along the crystallographic *c* axis. UV−vis diffuse reflectance spectra identify Ag_2GeS_3 as a semiconductor with an optical indirect band gap of 2.04 eV. Thermal analysis inside a sealed tube indicates that Ag_2GeS_3 undergoes several phase transitions but reforms upon cooling after heating to 1000 °C. Thermoelectric conductivity measurements show that Ag_2GeS_3 exhibits glass-like ultralow lattice thermal conductivity of 0.26 W/m·K at 300 K and 0.22 W/m·K at 380 K. The theoretical calculation of lattice thermal conductivity based on density functional theory using the modified Debye−Callaway model shows a good qualitative agreement with experimental results between 50 and 400 K. A combination of the zig-zag atomic arrangement that decorates the crystal structure, electronic structure features dominated by the hybridization of Ag−S bonds near the Fermi energy, and nearly flat or dispersion-less low-energy optical phonon branches where Ag acts as the rattler atom provides plausible reasons for the observed ultralow lattice thermal conductivity.

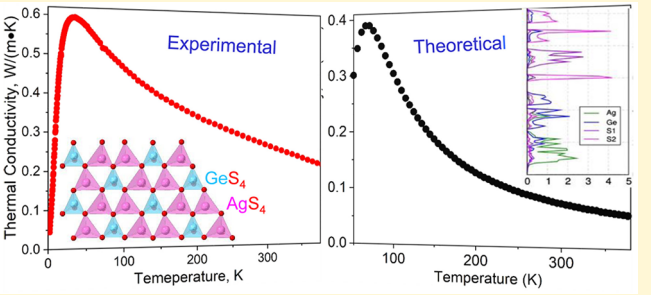

INTRODUCTION

Thermoelectric materials have been of great interest for a number of decades due to their ability to generate power, such as recycling of heat waste.[1] A thermoelectric device consists of p-type (hole conduction) and n-type (electron conduction) semiconductors, which transform heat into electricity (Seebeck effect) or convert electricity into cooling technology (Peltier effect).[2−4] The effectiveness of thermoelectric materials is determined by the figure of merit $zT = S^2\sigma T/\kappa_{total}$, where *S* is the Seebeck coefficient, σ is the electrical conductivity, *T* is the temperature, and κ is the thermal conductivity. The κ_{total} is the summation of the lattice thermal conductivity (κ_l) and the electrical thermal conductivity (κ_e). A large zT is indicative of an efficient thermoelectric material, which requires a large power factor (PF = $S^2\sigma$) and small κ_{total}.

Among the reported compounds in A−X−Q (A = Ag and Cu; X = Si, Ge, and Sn; and Q = S, Se, and Te) system, argyrodites with a general formula $A_{12-n}X^{n+}Q_6$ (A = Ag and Cu; X = Si, Ge, and Sn; and Q = S, Se, and Te) have been intensively studied as thermoelectric materials due to glass-like ultralow κ_{total} or κ_l.[5−8] Recent reported examples are Ag_8SnSe_6 [$\kappa_l \sim 0.2$ W/(m·K), $zT_{max} = 0.9-1.2$],[9−11] Ag_8GeTe_6 [$\kappa_{total} = 0.25$ W/(m·K), $zT = 0.48$ at 703 K],[12] Ag_8SiTe_6 [$\kappa_{total} = 0.23$ W/(m·K), $zT = 0.48$ at 800 K],[13] and Cu_8GeSe_6 [$\kappa_l = 0.2-0.3$ W/(m·K), $zT = 0.5$ at 750 K].[14] Most argyrodites A_8XQ_6 crystallize in non-centrosymmetric polar space groups ($Pmn2_1$, $Pna2_1$, and $P6_3mc$) at room temperature and transform into centrosymmetric cubic structures at high temperatures ($F\bar{4}3m$).[15,16]

Another promising series of thermoelectric materials in the A−X−Q system is the A_2XQ_3 series (A = Ag and Cu; X = Si, Ge, and Sn; and Q = S, Se, and Te). The resistivity, Hall effect, and semiconducting features were only briefly studied for some compounds in the 1960s and 1970s.[17−21] Recently, $Cu_2Sn_{0.9}In_{0.1}Se_3$ with a polar crystal structure (space group *Cc*) was reported with $\kappa_{total} = 1.0$ W/(m·K), $\kappa_l = 0.4$ W/(m·K), and $zT = 1.14$ at 850 K.[22] Cu_2GeSe_3 (space group *Imm*2) was reported with a $\kappa_{total} = 0.67$ W/(m·K) and $zT = 0.5$ for the Ga-doped sample ($Cu_2Ge_{0.93}Ga_{0.07}Se_3$) at 745 K.[23] The original orthorhombic crystal structure (space group *Imm*2) of Cu_2GeSe_3 was later re-determined to be a monoclinic crystal

Received: April 6, 2022
Revised: June 21, 2022
Published: July 15, 2022

structure with the polar space group *Cc*.[24] The low κ_l of Cu_2GeSe_3 is associated with a weak Cu−Se covalent bond[25] or the strong anharmonic phonon scattering.[23] The mechanism of ultralow κ_l in argyrodites A_8XQ_6 (A = Ag and Cu; X = Si, Ge, and Sn; and Q = S, Se, and Te) is related to the low frequency of the optical phonon, complex structure (240 atoms) with superionic character, weak chemical bond, and heavy element.[5,9,10] Ag_2GeS_3 also adopts a closely related polar crystal structure (space group $Cmc2_1$),[26] and we expect that Ag_2GeS_3 could show a low κ value, but the underlying mechanism might be different from that of Cu_2GeSe_3 and A_8XQ_6. Up to now, the thermoelectric properties of Ag_2GeS_3 are yet unknown.

In this article, we report the synthesis and characterization of a metastable polycrystalline Ag_2GeS_3 compound. We determine its crystal structure by in situ synchrotron X-ray diffraction, phase stability by differential scanning calorimetry (DSC), optical band gap by UV−vis spectroscopy, and high- and low-temperature thermal conductivities by laser flash analysis and physical property measurement system, respectively.

EXPERIMENTAL SECTION

Starting Materials and Synthesis. Ag_2GeS_3 polycrystalline samples were prepared using the conventional solid-state method with binary sulfides (Ag_2S and GeS_2) as starting materials. Ag_2S (99.9 wt %, Alfa Aesar) and GeS_2 (>99 wt %, MP Biomedicals) were stored and used inside an argon-filled glovebox with a low concentration of O_2 and H_2O (<0.5 ppm). A mixture of Ag_2S and GeS_2 with a stoichiometric molar ratio was thoroughly ground and pressed into a 6 mm diameter pellet, which was transferred to a 7.5 mm inner diameter (ID) quartz tube that was sealed under vacuum ($\sim 10^{-3}$ Torr). The sealed quartz ampule was heated in a box furnace to 1000 °C over 12 h and retained at that temperature for 168 h. After that, the furnace was turned off and cooled to room temperature within a few hours.

Laboratory and In Situ Synchrotron Powder X-ray Diffraction. Room-temperature powder X-ray diffraction (PXD) was initially collected for 1 h with a benchtop Miniflex-600 powder X-ray diffractometer (Cu Kα, λ = 1.5418 Å) with the 2Θ range from 10 to 70°. The room-temperature synchrotron powder X-ray diffraction (SPXD) pattern was collected in a capillary at 11-BM beamline (λ = 0.45790 Å) with the 2Θ range from 0.5 to 42° at the Advanced Photon Source, Argonne National Laboratory (APS-ANL). In situ SPXD experiments were carried out in an open-end quartz tube with an outer diameter (OD) of 1.1 mm under the argon flow at 17-BM beamline (λ = 0.24138 Å) from room temperature to 1000 °C at the APS-ANL.

Thermal Analysis. The thermal stability of Ag_2GeS_3 was assessed by the DSC with a model STA 449 F3, Netzsch TG/DSC instrument. Because of the potential reactions between the sample and the platinum sample stage, the sample was sealed under vacuum (<10^{-5} Torr) in a small quartz ampule (length = 11.5 mm, OD = 7 mm, and ID = 5 mm). A hydrogen torch was used to seal the tube in order to avoid warping the ampoule and minimize any destruction of the sample. An empty ampule was similarly prepared for use as the blank. Calorimetry was performed using a SiC furnace with the same heating and cooling rate of 10 °C/min between room temperature and 1000 °C. After the DSC measurement, the ampule was broken, and the sample was analyzed by PXD on a zero-background quartz sample stage using a Cu Kα source with a Ni filter (D8 ADVANCE ECO, Bruker).

Consolidation. Polycrystalline powders of Ag_2GeS_3 were consolidated by spark plasma sintering (SPS) (Dr. Lab Sinter Jr., Fuji Corp.) in a 12.7 mm diameter unjacketed graphite die or a 10 mm diameter die with an outer jacket to help prevent breakage (Cal Nano). Samples were prepared in an argon-filled glovebox (H_2O, O_2 < 0.5 ppm) and pressed under an active vacuum to avoid oxidation of the sample at elevated temperatures. A dense black pellet (12.7 mm dia.) was obtained after polycrystalline powders were slowly heated to 450 °C and held at 450 °C for 20 min under a constant force of 10.7 kN (21.1 MPa). Similarly, a chalky red pellet (10 mm dia.) was achieved when polycrystalline powders were held for 20 min at 250 °C under a constant force of 8 kN (25.5 MPa). A 4.5 mm dense pellet (>91% density) was prepared after being held at 250 °C for 4 h under 4 GPa using a Walker-type high-pressure instrument. The obtained pellets were also examined with PXD.

High-Temperature Thermal Conductivity. High-temperature thermal diffusivity was conducted on the consolidated 12.7 mm pellet from room temperature to 450 °C through laser flash analysis (LFA) 457 MicroFlash, NETZSCH. The sample was leveled using progressively finer sandpaper and then coated with a thin layer of graphite. LFA measurements were carried out under active argon flow to avoid oxidation. Thermal conductivity (κ) ($\kappa = D \times \rho \times C_p$) was then calculated from the measured density (ρ) using the Archimedes method, along with measured thermal diffusivity (D) and heat capacity (C_p), which were calculated using the Dulong−Petit method. Because of the thermal degradation of Ag_2GeS_3 to $Ag_{10}Ge_3S_{11}$ through the cycling process, the latter phase was used for the C_p calculation.

Low-Temperature Thermal Conductivity. Thermoelectric properties were measured on half of the dense pellet (4.5 mm) of phase-pure Ag_2GeS_3 using the thermal transport option of the Quantum Design physical property measurement system (PPMS). Temperature-dependent thermal conductivity data were collected from 380 to 1.8 K with a two-probe method. Electrical measurement was also attempted on the dense pellet but failed due to the high sample resistance and the power limits of the excitation source in the standard PPMS resistivity option.

Chemical Analysis. Elemental analyses of Ag_2GeS_3 polycrystalline samples were carried out with a Zeiss-Sigma field emission scanning electron microscope (SEM) equipped with an Oxford INCAEnergy 250 energy-dispersive X-ray spectroscopy (EDX) microanalysis system.

UV−Vis Diffuse Reflectance. Optical UV−vis diffuse reflectance spectra were collected using a Shimadzu UV-2600 Plus spectrometer. The polycrystalline Ag_2GeS_3 sample was measured in the range of 185 to 900 nm with barium sulfate as a non-absorbing reflectance reference. The derived UV−vis absorbance spectra $[F(R)]$ from reflectance spectra were obtained according to the Kubelka−Munk equation, $F(R) = a/S = (1 - R)^2/2R$, where a is the absorption coefficient, S is the scattering coefficient, and R is the diffuse reflectance. The band gap is estimated by extrapolations of the linear region of the $[F(R)h\nu]^n$ versus $h\nu(E)$ curve, where $n = 2$ and $n = 1/2$ correspond to direct and indirect allowed transitions, respectively.

Computation Methods. First-principles calculations were performed based on density functional theory (DFT) as implemented in the open-source plane-wave pseudopotential code, Quantum ESPRESSO (QE).[27] We chose the generalized gradient approximation (GGA) and PBEsol exchange−correlation functional for all ground-state calculations.[28,29] The ultrasoft pseudopotential optimized in the Rappe−Rabe−Kaxiras−Joannopoulos scheme was used to treat the core and valence electrons.[30,31] The kinetic energy cutoff was set to 816 eV, and the Brillouin zone was sampled using a Γ-centered Monkhorst−Pack (MP) mesh for all calculations.[32] During the geometry optimization using variable cell relaxation implemented with the Broyden−Fletcher−Goldfarb−Shanno algorithm, the convergence thresholds were set at a force equal to or less than 2 meV/Å, using a Monkhorst−Pack k-mesh size of 6 × 10 × 12. Self-consistent field (SCF) calculations were carried out, followed by non-self-consistent field calculations (using a denser k-mesh of 12 × 16 × 18) to calculate the electronic density of states (DOS) and projected DOS (PDOS) based on the optimized crystal structure from QE.

Since the mean-field DFT-GGA approximation is known to underestimate the fundamental band gap, we used the many-body perturbation theory with G_0W_0 approximation as implemented in the Yambo code to obtain the quasi-particle correction.[33,34] The ground-

https://doi.org/10.1021/acs.chemmater.2c01050
Chem. Mater. 2022, 34, 6420−6430

state property for the G_0W_0 calculation is obtained from QE using the GGA exchange−correlation functional and SG15-optimized norm-conserving Vanderbilt pseudopotentials.[35] The kinetic energy cutoff for wavefunctions and charge densities was set to 816 and 3265.4 eV, respectively. A Γ-centered Monkhorst−Pack *k*-point mesh of size 4 × 4 × 4 was used for both SCF and NSCF calculations. In the Yambo code, the plasmon-pole approximation for the inverse dielectric function was applied. The screening matrix size (response block size) was set to 5 Ry (68.03 eV). A total of 260 unoccupied bands were used in the polarization function and self-energy integration to converge the correlation part of self-energy. To accelerate the convergence, the closure relation technique developed by Bruneval and Gonze was applied in the G_0W_0calculation.[36]

Phonon calculations were carried out based on the finite displacement method using Phonopy.[37] Supercells of size 2 × 2 × 2 were constructed to generate atomic displacements. Atomic forces of supercells associated with the systematic set of displacements were then calculated using QE. Born-effective charge tensors were calculated using QE linear response theory, which was taken into consideration to add the non-analytical term correction in the phonon dispersion calculation. The above steps of the phonon calculations were performed for three structures: one at the equilibrium volume and the other two at slightly smaller (−0.4%) and larger (+0.4%) volumes. Finally, the temperature-dependent lattice thermal conductivity (κ_l) calculations were performed using the modified Debye−Callaway model as implemented in the AICON code.[38] Despite the limitations, such as the use of the classical Boltzmann distribution to describe the phonon behavior as opposed to the Bose−Einstein distribution and treating the optical branch as a longitudinal acoustic branch, AICON provides a computationally efficient (albeit qualitative) route to calculate the κ_l of complex solids.

RESULTS AND DISCUSSION

Synthesis and Crystal Structure. The Ag_2GeS_3 phase can be prepared directly by annealing elements or a mixture of binary Ag_2S and GeS_2 precursors.[26,39] According to the phase diagram of Ag_2S−GeS_2, Ag_2GeS_3 is a metastable phase that only exists at a higher temperature above 525 °C.[40] To prevent the loss of S, we adopted the synthesis with binary precursors with the heating profile of a previous report on preparing glassy Ag_2GeS_3,[41] in which case, binary Ag_2S and GeS_2 were used as starting materials, and the glassy phase was achieved after quenching the ampule in water. We modified the synthesis by cooling the ampule along the furnace after heating it at 1000 °C for 7 days. The experimental PXD pattern matches the theoretical pattern of Ag_2GeS_3 with the polar space group $Cmc2_1$ (Figure S1).

The crystal structure of Ag_2GeS_3 ($Cmc2_1$) consists of layers of AgS_4 and GeS_4 tetrahedra in the *ab* plane, which stack along the crystallographic *c* axis via corner-sharing in a zig-zag way (Figure 1). In each layer in the *ab* plane, one GeS_4 tetrahedron is corner-shared with six AgS_4 tetrahedra, while one AgS_4 tetrahedron is corner-shared with three AgS_4 and three GeS_4 tetrahedra alternately, as shown in Figure 1c. GeS_4 tetrahedra are separated in the *ab* plane, but they form zig-zag chains via corner-sharing along the crystallographic *c* axis. AgS_4 tetrahedra form zig-zag chains along both crystallographic *b* and *c* axes. The crystal structure of Ag_2GeS_3 is different from that of Ag_8GeS_6, in which GeS_4 tetrahedra are isolated and connected to Ag and S atoms to form a three-dimensional framework. For the eight Ag atoms in one unit cell of the Ag_8GeS_6 crystal structure, three Ag atoms form AgS_4 tetrahedra, four Ag atoms are coordinated with three S atoms (AgS_3), and one Ag atom is linked with two S atoms (AgS_2).

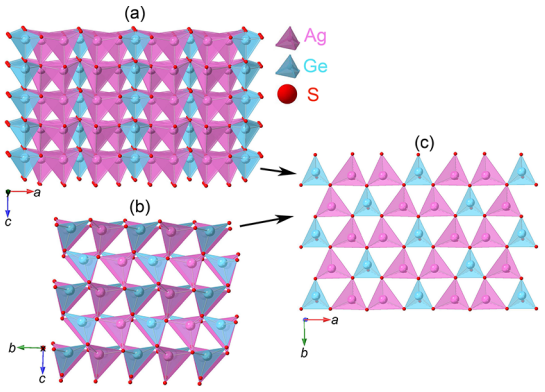

Figure 1. Perspective view of the crystal structure of Ag_2GeS_3 ($Cmc2_1$) viewed along the *b* axis (a), *a* axis (b), and a layer in the *ab* plane (c). Color code: Ag = light pink, Ge = light blue, and S = red.

To verify the reported crystal structure and investigate further details, Rietveld refinement was performed based on the room-temperature SPXD data. Careful examination of the high-resolution SPXD pattern identifies a small amount of impurity GeS_2 (2Θ = 4.57, 4.68, and 5.04°), reflections of which are marked with asterisks in Figure 2. Refinements were

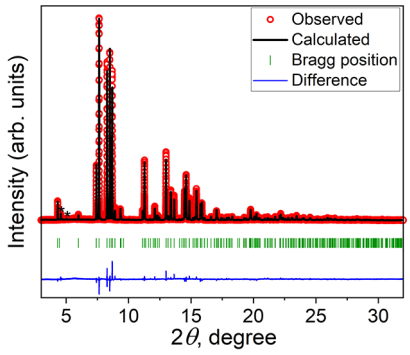

Figure 2. Rietveld refinement of SPXD of Ag_2GeS_3 (space group $Cmc2_1$, λ = 0.45790 Å) with the observed data (red), calculated pattern (black), difference between the observed and calculated patterns (blue), and Bragg position (green). Asterisks (*) represent the reflections of impurity GeS_2.

carried out with the previously reported crystal structures of Ag_2GeS_3 and GeS_2 as the initial models. The overall fitting and refinements are good (Figure 2). The mass fractions of the major phase Ag_2GeS_3 ($Cmc2_1$) and impurity GeS_2 ($Fdd2$) are 98.74 and 1.26%, respectively. Selected structural parameters of Rietveld refinement of Ag_2GeS_3 and GeS_2 are listed in Tables 1 and S1, respectively. The refined anisotropic displacement parameter (B) is given in Table S2. For the major phase Ag_2GeS_3, the unit cell parameters were determined to be a = 11.78794(2) Å, b = 7.07517(1) Å, c = 6.34337(1) Å, and V = 529.047(1) Å^3, which are close to the previously reported values, a = 11.791(5) Å, b = 7.079(3) Å, c = 6.344(3) Å, and V = 529.5(4) Å^3.[26] The refined atomic positions based on SPXD data show deviation from the previously reported values based on PXD, especially on the Ge (y), S1 (z), and S2 (y) sites (Table 1), which results in different Ag−S and Ge−S bond distances as shown in Table 2. The atomic position is closely related to the intensity of the X-ray pattern, which is affected by the setup of the X-ray measurement. The SPXD data were collected on the sample

https://doi.org/10.1021/acs.chemmater.2c01050
Chem. Mater. 2022, 34, 6420−6430

Table 1. Selected Structural Parameters of Rietveld Refinement of Ag_2GeS_3

sample	Ag_2GeS_3
empirical formula	Ag_2GeS_3
temperature	300 K
mol. wt, g/mol	384.57
density (calculated), g/cm^3	4.828
wavelength, λ	0.45790 Å
space group, #	$Cmc2_1$, #36
Z	4
lattice parameters	a = 11.78793(2) Å, b = 7.07517(1) Å, c = 6.34337(1) Å, V = 529.047(1) Å^3
Rietveld criteria of fit	R_p = 8.05%, R_{wp} = 10.0%, R_{exp} = 6.01%, $R_{f\text{-}factor}$ = 8.46%, R_{Bragg} = 8.74%, χ^2 = 2.77

site, Wyckoff symbol	x, y, z (this work) x, y, z (reported values)[26]
Ag, 8b	0.1554(1), 0.8677(1), −0.02(2) 0.152, 0.846, −0.027
Ge, 4a	0, 0.3445(2), −0.04(2) 0, 0.405, −0.048
S1, 8b	0.1561(2), 0.7987(2), 0.36(2) 0.142, 0.806, 0.404
S2, 4a	0, 0.3582(4), 0.32(2) 0, 0.319, 0.311

that was put in a capillary. The observed atomic position difference from reported values may be due to different sample preparations for the X-ray measurement. The site occupancies of S1 and S2 were checked during the refinement, but the overall fitting remained the same with 1.5 and 1.2% vacancies, so the occupancies were fixed at unity.

As shown in Figure 1, the crystal structure is built with AgS_4 and GeS_4 tetrahedra. In the AgS_4 tetrahedra, Ag coordinates with three S1 atoms and one S2 atom, with four different Ag−S bond distances ranging from 2.4 to 2.63 Å (Table 2). In the GeS_4 tetrahedra, Ge coordinates with two S1 atoms and two S2 atoms. The two Ge−S1 bond distances are equal (2.19 Å), and the two Ge−S2 bond distances (2.28 and 2.2 Å) are close (Table 2). The Ag−S and Ge−S bond distances are reasonable and similar to those in the crystal structure of Ag_8GeS_6 and $Ag_{10}Ge_3S_{11}$.[42,43] The nearest Ag−Ag/Ge distances are also listed in Table 2. Based on the bond distances, AgS_4 tetrahedra are more distorted compared to GeS_4 tetrahedra. The distorted tetrahedra and zig-zag arrangement of tetrahedra explain the polar crystal structure of Ag_2GeS_3.

Thermal Stability. The thermal stability of the Ag_2GeS_3 compound was first studied via differential scanning calorimetry. The powder sample was sealed inside a small quartz ampule (OD = 7 mm) and heated/cooled between room temperature and 1000 °C at a rate of 10 °C/min. Because the sample was flame-sealed inside the quartz ampule, it was not possible to run a background subtraction with the empty sample ampule. The result of this is the sweeping baseline most evident in the heating segment of the measurement. The heating segment of the DSC measurement shows a small endothermic peak at 354 °C and two smaller endothermic peaks near 627 and 874 °C. Upon cooling, a large exothermic peak was observed at 564 °C, and another weaker exothermic peak was observed at 248 °C (Figure 3). The sample was then

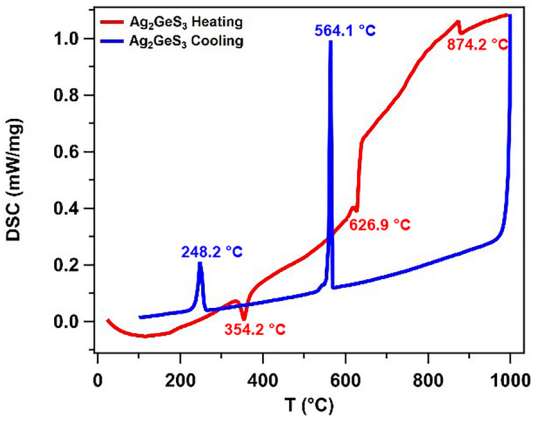

Figure 3. DSC curves of Ag_2GeS_3 with heating shown in red and cooling shown in blue. In this plot, upward peaks are exothermic, and those downward are endothermic.

examined with PXD. We found that when Ag_2GeS_3 was heated in a sealed quartz tube, its phase remained intact even after 1000 °C, as revealed by the PXD patterns shown in Figure 4.

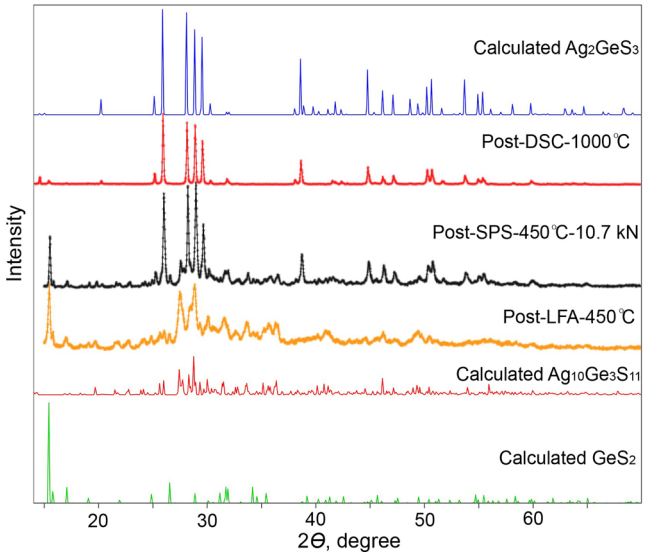

Figure 4. Experimental PXD patterns (Cu Kα, λ = 1.5418 Å) of samples after DSC, SPS, and LFA experiments in comparison with calculated PXD patterns of Ag_2GeS_3, $Ag_{10}Ge_3S_{11}$, and GeS_2.

Table 2. Selected Bond Distances in Ag_2GeS_3

Ag−S (Å)	this work	reported values[26]	Ge−S (Å)	this work	reported values[26]	Ag−Ag/Ge distance (Å)	this work	reported values[26]
Ag−S1	2.4(2)	2.50	Ge−S1	2.19(5)	2.26	Ag−Ag	3.66(1)	3.58
Ag−S1	2.48(6)	2.69	Ge−S1	2.19(5)	2.26	Ag−Ge	3.84(1)	3.60
Ag−S1	2.62(5)	2.75	Ge−S2	2.28(7)	2.15	Ge−Ge	3.8(1)	3.45
Ag−S2	2.63(7)	2.37	Ge−S2	2.2(2)	2.36			

https://doi.org/10.1021/acs.chemmater.2c01050
Chem. Mater. 2022, 34, 6420−6430

However, during the SPS process, the color of the pellet changed from red to black after pressing at 450 °C for 20 min under a constant force of 10.7 kN (21.1 MPa), suggesting a compositional change in the pellet. The post-SPS pellet was determined to be a mixed phase of Ag_2GeS_3, $Ag_{10}Ge_3S_{11}$, and GeS_2 (Figure 4). The pressure and high temperature (450 °C) cause part of the Ag_2GeS_3 pellet to be converted into $Ag_{10}Ge_3S_{11}$ and GeS_2 ($5Ag_2GeS_3 = Ag_{10}Ge_3S_{11} + 2GeS_2$). The minor sulfur loss likely prevented the reformation of Ag_2GeS_3 upon cooling. This mixed-phase pellet was heated up to 450 °C during the LFA measurement, and the post-LFA PXD suggests that the Ag_2GeS_3 phase completely disappears and converts into $Ag_{10}Ge_3S_{11}$ and GeS_2 (Figure 4).

Based on the observation of the behavior of this material during the SPS, we can attribute the first peak at 354 °C observed in DSC to the conversion of Ag_2GeS_3 to $Ag_{10}Ge_3S_{11}$ and GeS_2. The peak near 627 °C may be related to the melting of that $Ag_{10}Ge_3S_{11}$ and GeS_2 mixture. The transition near 874 °C may be the melting of the remaining GeS_2. The strong exothermal peak at 564 °C observed in the DSC cooling process may be related to the reaction forming $Ag_{10}Ge_3S_{11}$ and GeS_2 from the melt. The recrystallization of Ag_2GeS_3 from that mixture corresponds to the exothermic peak at 248 °C. The offset between events in heating and cooling is due to the thickness of the quartz ampule, which leads to some delay between the temperature of the outside of the ampule and the actual temperature of the sample within.

To further understand the phase stability of Ag_2GeS_3 and the observed conversion from Ag_2GeS_3 to $Ag_{10}Ge_3S_{11}$ and GeS_2, we carried out the in situ SPXD. The in situ SPXD experiment was carried out in an open-ended small quartz tube under argon flow from room temperature to 1000 °C while collecting data every 10 °C. The Ag_2GeS_3 phase is stable below 327 °C but decomposes into Ag_2S and GeS_2 between 327 and 357 °C (Figure 5). Above 357 °C, $Ag_{10}Ge_3S_{11}$ begins to form, and the pure phase $Ag_{10}Ge_3S_{11}$ compound is observed at 627 °C. Between 627 and 677 °C, the $Ag_{10}Ge_3S_{11}$ phase converts into Ag_8GeS_6 and glassy GeS_2 and Ag_2S ($Ag_{10}Ge_3S_{11} = Ag_8GeS_6 + 2GeS_2 + Ag_2S$), with polycrystalline Ag_8GeS_6 observed at 677 °C. The polycrystalline Ag_8GeS_6 becomes a glassy phase above 827 °C. During the cooling process, only a few peaks were observed below 850 °C, which cannot be identified as known binary or ternary compounds in the Ag−Ge−S system (Figure S2). Overall, the Ag_2GeS_3 phase is not observed after the in situ SPXD experiment, which is in contrast to the DSC experiment. It is worth noting that the in situ SPXD experiment was carried out in an open-end quartz tube while the DSC experiment was performed in the sealed quartz tube, which may be the reason for the discrepancy between the two experiments. The proposed decompositions of Ag_2GeS_3 to $Ag_{10}Ge_3S_{11}$ and GeS_2 based on DSC and in situ SPXD experiments occur at much lower temperatures compared to the temperature (525 °C) that Ag_2GeS_3 forms from $Ag_{10}Ge_3S_{11}$ and GeS_2 according to the Ag_2S−GeS_2 phase diagram.[40] The observed difference indicates that the stability of Ag_2GeS_3 is very sensitive to the experimental conditions, and in future work, it will be intriguing to explore how the phase diagram can change as a function of experimental conditions.

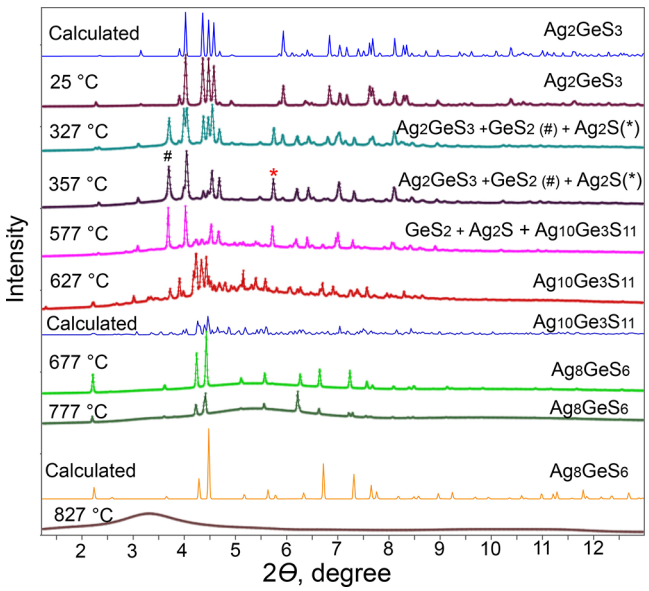

Figure 5. Selected in situ SPXD patterns of Ag_2GeS_3 obtained while heating from 25 to 1000 °C (λ = 0.24138 Å).

Chemical Analysis. SEM−EDX measurements were carried out on the prepared an Ag_2GeS_3 pellet (10 mm dia.). The average size of the particles is less than 10 μm (Figure S3). Elemental mapping of a small area of the pellet indicates that the Ag, Ge, and S elements are homogeneously distributed throughout the sample (Figure 6). The calculated molar ratio of Ag/Ge/S is equal to 1.95:1.0:2.64, which is close to the expected ratio of 2:1:3, but with a small amount of S deficiency which may be due to the sulfur loss during the hot-pressing process.

Thermal Conductivity. High-temperature κ_{total} was measured on the 12.7 mm dense pellet, which is a mixed phase of Ag_2GeS_3, $Ag_{10}Ge_3S_{11}$, and GeS_2 at room temperature. Initial results on the pellet showed a large hysteresis on cooling due to compositional changes. The second measurement cycle is shown in Figure 7a after the composition was relatively stable. The κ_{total} is 0.37 W/(m·K) at 320 K, and it decreases as the temperature increases (Figure 7a). At 695 K, κ_{total} reaches the lowest value of 0.30 W/(m·K). The contribution of κ_e to the κ_{total} value is negligible. Therefore, the κ_{total} ($\kappa_l + \kappa_e$) may be contributed entirely by the κ_l. The κ_l is very low even though the results were obtained in a mixed phase. σ and S measurements could not be performed because the sample was too resistant to be measured with an LSR-3 instrument.

To obtain a more accurate κ_{total} for Ag_2GeS_3, a phase-pure 4.5 mm dense pellet (>91% density) with a thickness of ~1.5 mm was obtained at 4 GPa and 250 °C for 4 h. Half of the pellet was used for collecting low-temperature data of κ_{total} from 380 to 1.8 K with a two-probe method. Between 380 and 35 K, the value of κ increases as the temperature decreases, which is in agreement with what is expected for $1/T$ phonon heat transport (Figure 7b).[44] At 380 K, the value of κ_{total} is 0.22 W/m·K, and it increases to 0.26 W/m·K at 300 K. The obtained ultralow κ_{total} values in the low-temperature range (380 to 1.8 K) are consistent with those in the high-temperature (300 to 723 K) κ_{total} experiment. The κ_{total} reaches a maximum value of 0.60 W/(m·K) at a low temperature of 35 K. Between 35 and 2 K, κ_{total} decreases as the temperature decreases. The peak (at 35 K) where κ transforms from $1/T$ to the T^3 phonon behavior has also been observed in the similar temperature regime in other similar compounds such as $Cu_2Ga_xGe_{1-x}Se_3$ ($0 \le x \le 0.1$),[23] $Ge_{0.9}Mg_{0.04}Bi_{0.06}Te$,[45] Cu_4TiSe_4,[46] and $AgCrSe_2$.[47] Low-temperature σ and S were

https://doi.org/10.1021/acs.chemmater.2c01050
Chem. Mater. 2022, 34, 6420−6430

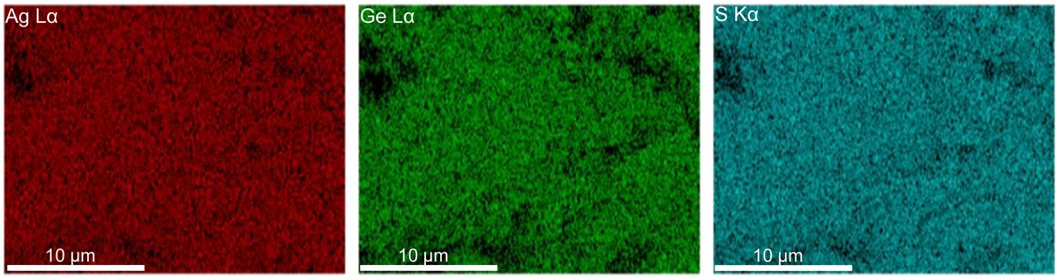

Figure 6. EDX elemental mapping of an Ag_2GeS_3 pellet.

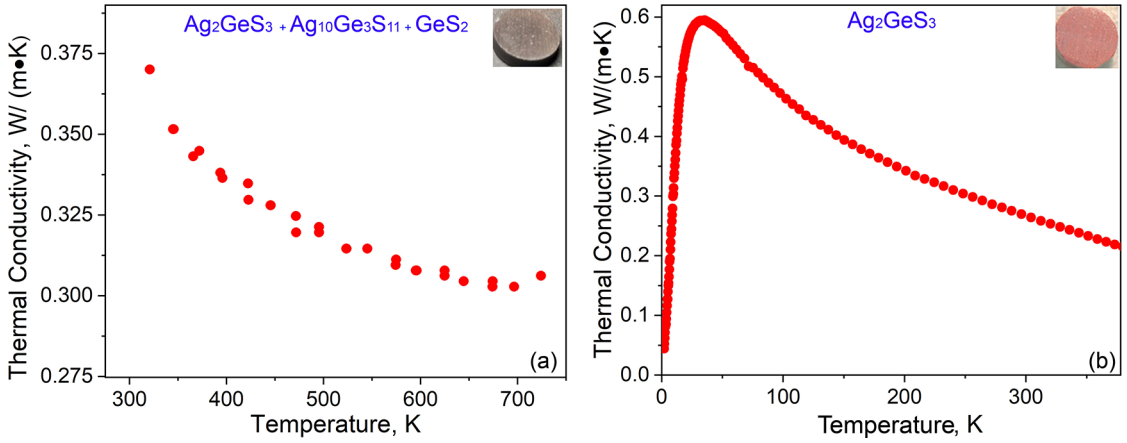

Figure 7. Temperature-dependent κ_{total} measured on the pellet of (a) Ag_2GeS_3, $Ag_{10}Ge_3S_{11}$, and GeS_2 mixture; and (b) phase-pure Ag_2GeS_3.

not measured due to the high sample resistivity and the power limits of the excitation source and sensitivity of the voltage measurement, respectively, in the standard PPMS resistivity option.

The value of κ_{total} of Ag_2GeS_3 is smaller than that [$\kappa_{total} \sim 0.7-1$ W/(m·K)] of Cu_2XQ_3 (X = Ge and Sn; Q = S and Se) and comparable with that [$\kappa_{total} \sim 0.2-0.5$ W/(m·K)] of argyrodites A_8XQ_6 (A = Ag and Cu; X = Si, Ge, and Sn; and Q = S, Se, and Te).[18,48] Due to the high resistivity of Ag_2GeS_3, κ_{total} is equal to $\kappa_l = 1/3(C_v \cdot \nu \cdot l)$, where C_v is the heat capacity at a constant volume, ν is the sound velocity, and l is the phonon mean free path, which is determined by phonon scattering. The low κ_l of Cu_2GeSe_3 has been ascribed to a low Debye temperature caused by the weak Cu−Se covalent bond[25] or the strong anharmonic phonon scattering related to high bonding anharmonicity.[23] Ultralow κ_l of argyrodites A_8XQ_6 (A = Ag and Cu; X = Si, Ge, and Sn; and Q = S, Se, and Te) has been explained by the low sound velocity (due to weak chemical bonds and heavy elements), the low frequency of the optical phonons, disordered caused by superionic character, and a large unit cell with 240 atoms.[5,9,10] Compared to Cu_2GeSe_3 and argyrodites A_8XQ_6, the ultralow κ_l in Ag_2GeS_3 is unexpected but interesting. Similar to Cu_2GeSe_3 and A_8XQ_6, the Ag−S bonding in Ag_2GeS_3 is covalent. However, the Ag_2GeS_3 compound has a smaller unit cell with fewer atoms and lacks heavy atoms like Sn. The ultralow κ_l of Ag_2GeS_3 is also comparable with other reported examples of chalcogenides (Table 3), which can be categorized as glass-like materials.

UV−Vis Diffuse Reflectance. UV−vis diffuse reflectance spectra were collected to determine the optical band gap of Ag_2GeS_3. The derived UV−vis absorbance spectra [$F(R)$] from reflectance spectra were obtained according to the Kubelka−Munk equation $F(R) = a/S = (1 - R)^2/2R$, where a is the absorption coefficient and S is the scattering coefficient and R is the diffuse reflectance.[59] Because $F(R)$ is proportional to a, the Tauc equation $(ah\nu)^n = A(h\nu - E_g)$ can be represented as $[F(R)h\nu]^n = A(h\nu - E_g)$, which is then used for the band gap analysis, where A is a constant and $n = 2$ and $n = 1/2$ correspond to direct and indirect allowed transitions, respectively.[60] Based on the $[F(R)h\nu]^n$ versus $h\nu(E)$ curves, the extrapolations of the linear regions yield the $E_g^{direct} = 2.13$ eV (Figure S4) and $E_g^{indirect} = 2.04$ eV (Figure 8). A previous report of electronic band structure calculations with different methods indicates that Ag_2GeS_3 is an indirect semiconductor with the largest theoretical band gap of 1.30 eV.[39] The

Table 3. Examples of Chalcogenides with Ultralow κ_l

compound	κ_l at 300 K, W/(m·K)	references
Ag_8GaSe_6	0.15	49
$AgSb_{0.94}Cd_{0.06}Te_2$	0.16	50
Cs_4TiSe_4	0.19	46
$CsAg_5Te_3$	0.18 (0.14 at 727 K)	51
$AgCrSe_2$	0.4	47
Ag_8SnSe_6	0.2	9, 11
Ag_2GeS_3	0.26	this work
Ag_8GeTe_6	0.25	12
Ag_9TlTe_5	0.23[a]	52
Tl_3VSe_4	0.3	53
$In_{0.997}Te$	0.43 (0.3 at 673 K)	54
SnSe	0.5−0.7 (0.23 at 973 K)	55
Cu_3SbSe_3	0.5	56
$AgSbTe_2$	0.5	50
$Cu_{1.98}Se$	0.6[b] (0.4−0.6 at 850−1000 K)	57
$Yb_{14}MnSb_{11}$	0.7[a]	58

[a]Value is reported for κ_{total}. [b]Data are measured at 400 K.

https://doi.org/10.1021/acs.chemmater.2c01050
Chem. Mater. 2022, 34, 6420−6430

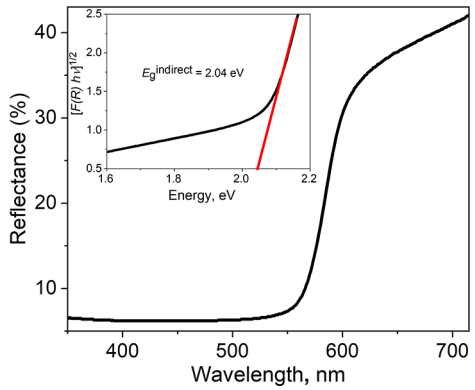

Figure 8. UV−vis diffuse reflectance spectra and Tauc plot (inset) of Ag_2GeS_3.

obtained optical indirect band gap ($E_g^{indirect}$ = 2.04 eV) here is close to the reported energy band gap estimated from intrinsic photoconductivity (2.16 eV) and absorption edge (1.98 eV).[39]

Theoretical Lattice Thermal Conductivity Calculations. Based on seminal studies in literature,[61−65] several factors have been shown to contribute to large anharmonicity in crystals, leading to ultralow κ_l: (1) Crystal structure, where layered or zig-zag geometries have been shown to promote phonon scattering, leading to ultralow κ_l.[66] (2) An electronic band structure, where the presence of the ns^2 lone-pair effect has been shown to result in increased lattice deformation, leading to soft phonons and large anharmonicity.[61] (3) A phonon band structure, where the presence of flat, non-dispersive lower optical and acoustic phonon modes in the phonon dispersion curves and low group velocities contributes to larger anharmonicity.[61]

In Ag_2GeS_3, the Ag and Ge atoms are fourfold coordinated by S atoms, which in turn are formed as infinite zig-zag chains (Figure 1). Thus, the crystal structure appears to host the necessary topology that favors ultralow κ_l. Table 4 provides the

Table 4. Leading Diagonal Terms in the Born-Effective Charge Tensor Data from the Linear Response Theory for Each of the Crystallographically Unique Lattice Sites in the Orthorhombic Ag_2GeS_3 Structure[a]

atom	Z^*_{xx}	Z^*_{yy}	Z^*_{zz}
Ag	1.051	1.026	1.033
Ge	2.929	2.918	3.438
S1	−2.130	−1.370	−1.270
S2	−0.786	−2.247	−2.997

[a]The nominal charge of Ag, Ge, and S in Ag_2GeS_3 is +1, +4, and −2, respectively.

dynamical Born-effective charge tensor data from the linear response theory (only the leading diagonal terms are shown). The Ag atoms appear to behave as expected (i.e., show predominantly ionic bonding) because the nominal charge (+1) is close to the dynamical charge. The Ge, S1, and S2 atoms deviate most from the nominal charge, indicating non-trivial chemical bonding in their coordination environment. In the $Cmc2_1$ structure, the Ag-atom coordinates with three S1 atoms and one S2 atom, whereas the Ge-atom coordinates with two S1 (shorter bond lengths) and two S2 atoms (longer bond lengths). The bond length data from experiments and DFT-optimized structures are given in Tables 2 and 5,

Table 5. Selected Bond Distances in Ag_2GeS_3 from the DFT-Optimized Crystal Structure (a = 11.68399 Å, b = 6.90581 Å, c = 6.43778 Å, and V = 519.4478 Å^3)

Ag−S (Å)		Ge−S (Å)		Ag−Ag/Ge distance (Å)	
Ag−S1	2.48303	Ge−S1	2.1902	Ag−Ag	3.63395
Ag−S1	2.49015	Ge−S1	2.1902	Ag−Ge	3.8652
Ag−S1	2.53398	Ge−S2	2.29732	Ge−Ge	3.93019
Ag−S2	2.51751	Ge−S2	2.35493		

respectively. We interpret that compared to AgS_4, the GeS_4 tetrahedron plays a relatively dominant role in impacting the dynamical charge of S2 atoms in the crystal structure. Among all the atomic sites in the structure, the S2 atom can be classified as having an anomalous dynamical charge (Table 4).

The electronic DOS is shown in Figure 9a. The electronic structure at the mean-field GGA-level confirms a band gap of 0.43 eV (an enlarged section of PDOS is provided in Figure S5), which is an underestimation of the actual band gap of 2.04 eV (Figure 8). This is a known deficiency of local and semi-local functionals that fail to capture the excited state property, such as the band gap.[67] The atom PDOS shows an overlap mostly between Ag 4d orbitals and S 3p orbitals below the Fermi energy (E_F). A large spectral weight associated with Ge 4p and S 3p hybridization is only found at about 5 eV below the E_F. Because of the lack of overlap between the Ge 4s orbitals and S 3p orbitals near the E_F, we infer that there is no dominant involvement of Ge−S bonds in determining the properties of Ag_2GeS_3.

In Figure 9b, we show two electronic band structures, where the calculations are performed at two levels of approximation: (1) at the mean-field DFT-GGA (PBE) level and (2) at the more accurate many-body DFT-G_0W_0 method. The DFT-G_0W_0 method predicts indirect and direct band gaps of 1.12 and 1.17 eV, respectively. While the DFT-G_0W_0 indirect band gap is in close agreement with the work of Reshak et al.,[39] who reported an indirect gap of 1.3 eV using the hybrid functional, the DFT-G_0W_0 method still underestimates the experimental indirect gap of 2.04 eV. We also note that the PDOS data shown in Figure 9a were computed using the ultrasoft pseudopotential (PBEsol), whereas the DFT-PBE band structure shown in Figure 9b was calculated using the norm-conserving pseudopotential (PBE). While the PDOS predicts a band gap of 0.43 eV, the band structure predicts an indirect gap of ∼0.50 eV. This is mainly due to the choice of two different pseudopotentials in our calculations. From Figure 9a, the Ag−S chemical bonds are perceived to be critical in deciding the average group velocities of low-frequency phonon modes. This is also confirmed by an investigation of the phonon dispersion curve (Figure 9c) and the phonon DOS (Figure 9d). The optical modes in the phonon dispersion curve (especially those in the low-frequency range) were found to be almost flat without much dispersion, as shown in Figure 9b. Our focus on the low-frequency modes is due to their key role as the heat-carrying phonons, where the presence of a flat feature is known to give rise to small lifetimes, leading to ultralow κ_l.[68] The noticeably large contribution from the Ag atoms to the low optical frequency flat modes in the phonon PDOS (Figure 9d) reveals its dominant role as the rattler in the crystal structure.

Molecular dynamics (MD) simulations can be used for the calculation of κ_l directly from the non-equilibrium MD or

https://doi.org/10.1021/acs.chemmater.2c01050
Chem. Mater. 2022, 34, 6420−6430

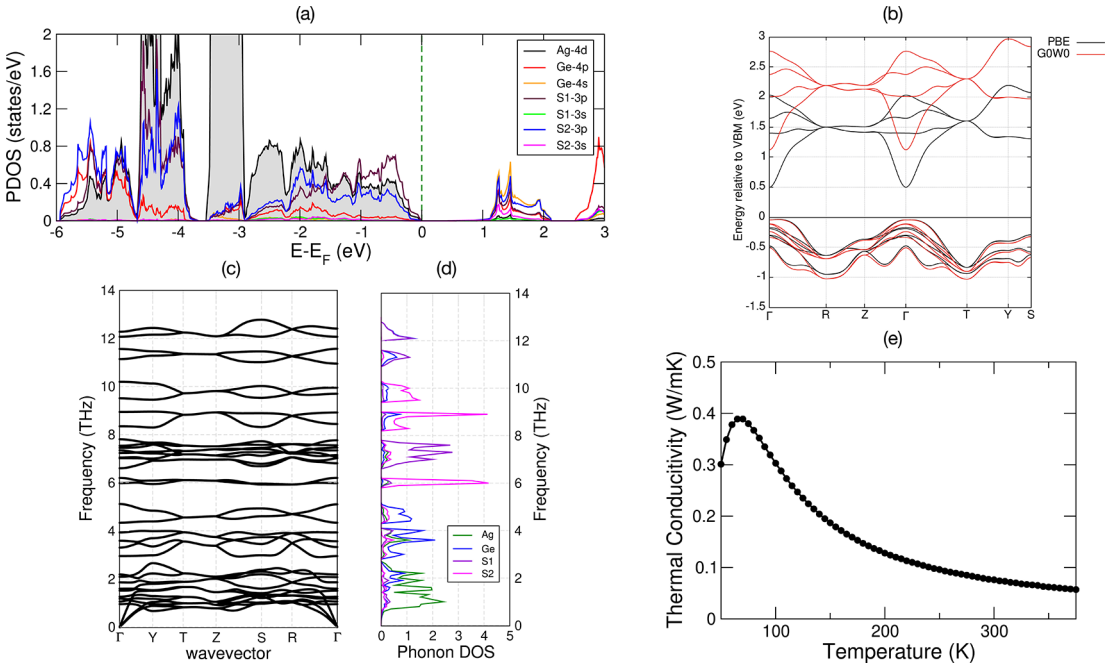

Figure 9. DFT results showing atom- and orbital-PDOS of Ag_2GeS_3 with the PDOS of the Ag 4d orbitals shaded in gray (a), electronic band structure at the less accurate DFT-PBE (black) and more accurate DFT-GW (red) approximations (b), phonon dispersion curve (c), phonon DOS (d), and calculated κ_l vs T using AICON (e). In (b), VBM (in the Y-axis) stands for valence band maximum.

based on the Green−Kubo method.[69−71] However, these simulations need large simulation cells to consider the finite size effect and a long simulation time to converge the autocorrelation function. Alternatively, the Boltzmann transport equation can be used for the calculation of κ_l using DFT. However, the calculation of the second-and third-order force constants is also expensive.[38] A feasible method that is both relatively inexpensive with respect to computational time and complexity is the modified Debye−Callaway model within the relaxation time approximation. This model could be used to calculate κ_l in the absence of experimental parameters. The AICON code implements the modified Debye−Callaway model for calculating κ_l. This model requires input parameters that can be directly calculated from the phonon dispersion curves within the quasi-harmonic approximation. The calculated κ_l versus temperature is given in Figure 9e, which shows a good qualitative agreement with experimental results above 50 K.

CONCLUSIONS

Metastable Ag_2GeS_3 has been successfully synthesized via the conventional solid-state method with starting materials Ag_2S and GeS_2. The polar crystal structure containing layers of corner-shared distorted AgS_4 and GeS_4 tetrahedra was confirmed by the Rietveld refinement of the synchrotron X-ray diffraction data. The ultralow lattice thermal conductivity of 0.26 W/m·K at 300 K and 0.22 W/m·K at 380 K was revealed by the low-temperature thermoelectric conductivity measurements, which is supported by the results of the theoretical calculations. The glass-like thermal conductivity is related to the localized modes of Ag and S atoms that contribute to the flat feature of lower frequency optical modes in the phonon dispersion curve, and the Ag 4d and S 3p orbitals overlap in the electronic PDOS. Ag_2GeS_3 is a special example of chalcogenides that show such low thermal conductivity that it is not related to the presence of heavy elements in the structure. Ag_2GeS_3 displays a wide indirect band gap of 2.04 eV and high electrical resistivity. Future improvement on the thermoelectrical properties of this glass-like material and related compounds (e.g., $Ag_{10}Ge_3S_{11}$) can be focused on enhancing the electrical conductivity via aliovalent dopants, which might provide a path forward for more efficient thermoelectrics.

ASSOCIATED CONTENT

Supporting Information

The Supporting Information is available free of charge at https://pubs.acs.org/doi/10.1021/acs.chemmater.2c01050.

Laboratory PXD pattern; refined anisotropic displacement parameter (B) of Ag_2GeS_3, refined structural parameters of second-phase GeS_2; SEM image of the surface of the Ag_2GeS_3 pellet, the Tauc plot of the direct optical band gap of Ag_2GeS_3, and an enlarged section of PDOS (PDF)

AUTHOR INFORMATION

Corresponding Authors

Prasanna V. Balachandran − *Department of Materials Science and Engineering and Department of Mechanical and Aerospace Engineering, University of Virginia, Charlottesville, Virginia 22902, United States;* orcid.org/0000-0002-7496-5521; Email: pvb5e@virginia.edu

Susan M. Kauzlarich − *Department of Chemistry, University of California, Davis, California 95616, United States;* orcid.org/0000-0002-3627-237X; Email: smkauzlarich@ucdavis.edu

Xiaoyan Tan − *Department of Chemistry and Biochemistry, George Mason University, Fairfax, Virginia 22030, United States;* orcid.org/0000-0002-1742-8252; Email: xtan6@gmu.edu

https://doi.org/10.1021/acs.chemmater.2c01050
Chem. Mater. 2022, 34, 6420−6430

Authors

Callista M. Skaggs − *Department of Chemistry and Biochemistry, George Mason University, Fairfax, Virginia 22030, United States*

Andrew P. Justl − *Department of Chemistry, University of California, Davis, California 95616, United States;* orcid.org/0000-0001-6332-4545

Ankita Biswas − *Department of Materials Science and Engineering, University of Virginia, Charlottesville, Virginia 22902, United States*

Peter E. Siegfried − *Department of Physics and Astronomy and Quantum Science and Engineering Center, George Mason University, Fairfax, Virginia 22030, United States;* orcid.org/0000-0002-0145-2899

Shunshun Liu − *Department of Materials Science and Engineering, University of Virginia, Charlottesville, Virginia 22902, United States*

Saul H. Lapidus − *X-ray Science Division, Advanced Photon Source, Argonne National Laboratory, Lemont, Illinois 60439, United States;* orcid.org/0000-0002-7486-4325

Wenqian Xu − *X-ray Science Division, Advanced Photon Source, Argonne National Laboratory, Lemont, Illinois 60439, United States*

Zachary T. Messegee − *Department of Chemistry and Biochemistry, George Mason University, Fairfax, Virginia 22030, United States;* orcid.org/0000-0001-9702-580X

Nirmal J. Ghimire − *Department of Physics and Astronomy and Quantum Science and Engineering Center, George Mason University, Fairfax, Virginia 22030, United States;* orcid.org/0000-0002-8474-4968

Complete contact information is available at: https://pubs.acs.org/10.1021/acs.chemmater.2c01050

Author Contributions

$^{\nabla}$C.M.S. and A.P.J. contributed equally.

Notes

The authors declare no competing financial interest.

■ ACKNOWLEDGMENTS

C.M.S., A.B., Z.T.M., P.V.B., and X.T. were supported by the 4-VA @ Mason project. A.P.J. and S.M.K. were funded through a National Science Foundation (NSF) grant DMR-2001156. The use of the Advanced Photon Source at Argonne National Laboratory was supported by the U. S. Department of Energy, Office of Science, Office of Basic Energy Sciences, under contract no. DE-AC02-06CH11357. N.J.G. acknowledges the support from the NSF CAREER award DMR-2143903. A.B. and P.V.B. thank Tao Fan for useful discussions about the AICON code. We thank Dr. David Walker (Columbia University) for pressing the dense pellet under high pressure.

■ REFERENCES

(1) Bell, L. E. Cooling, Heating, Generating Power, and Recovering Waste Heat with Thermoelectric Systems. *Science* **2008**, *321*, 1457−1461.

(2) Peltier, J. C. Nouvelles Expériences Sur La Caloricité Des Courants Électrique. *Ann. Chim. Phys.* **1834**, *56*, 371−386.

(3) Goldsmid, H. J.; Douglas, R. W. The Use of Semiconductors in Thermoelectric Refrigeration. *Br. J. Appl. Phys.* **1954**, *5*, 386−390.

(4) DiSalvo, F. J. Thermoelectric Cooling and Power Generation. *Science* **1999**, *285*, 703−706.

(5) Heep, B. K.; Weldert, K. S.; Krysiak, Y.; Day, T. W.; Zeier, W. G.; Kolb, U.; Snyder, G. J.; Tremel, W. High Electron Mobility and Disorder Induced by Silver Ion Migration Lead to Good Thermoelectric Performance in the Argyrodite Ag_8SiSe_6. *Chem. Mater.* **2017**, *29*, 4833−4839.

(6) Zhu, T. J.; Zhang, S. N.; Yang, S. H.; Zhao, X. B. Improved Thermoelectric Figure of Merit of Self-Doped $Ag_{8-X}GeTe_6$ Compounds with Glass-like Thermal Conductivity. *Phys. Status Solidi RRL* **2010**, *4*, 317−319.

(7) Lin, S.; Li, W.; Pei, Y. Thermally Insulative Thermoelectric Argyrodites. *Mater. Today* **2021**, *48*, 198−213.

(8) Yang, C.; Luo, Y.; Li, X.; Cui, J. N-Type Thermoelectric Ag_8SnSe_6 with Extremely Low Lattice Thermal Conductivity by Replacing Ag with Cu. *RSC Adv.* **2021**, *11*, 3732−3739.

(9) Li, W.; Lin, S.; Ge, B.; Yang, J.; Zhang, W.; Pei, Y. Low Sound Velocity Contributing to the High Thermoelectric Performance of Ag_8SnSe_6. *Adv. Sci.* **2016**, *3*, 1600196.

(10) Li, L.; Liu, Y.; Dai, J.; Hong, A.; Zeng, M.; Yan, Z.; Xu, J.; Zhang, D.; Shan, D.; Liu, S.; et al. High Thermoelectric Performance of Superionic Argyrodite Compound Ag_8SnSe_6. *J. Mater. Chem. C* **2016**, *4*, 5806−5813.

(11) Jin, M.; Lin, S.; Li, W.; Chen, Z.; Li, R.; Wang, X.; Chen, Y.; Pei, Y. Fabrication and Thermoelectric Properties of Single-Crystal Argyrodite Ag_8SnSe_6. *Chem. Mater.* **2019**, *31*, 2603−2610.

(12) Charoenphakdee, A.; Kurosaki, K.; Muta, H.; Uno, M.; Yamanaka, S. Reinvestigation of the Thermoelectric Properties of Ag_8GeTe_6. *Phys. Status Solidi RRL* **2008**, *2*, 65−67.

(13) Charoenphakdee, A.; Kurosaki, K.; Muta, H.; Uno, M.; Yamanaka, S. Ag_8SiTe_6: A New Thermoelectric Material with Low Thermal Conductivity. *Jpn. J. Appl. Phys.* **2009**, *48*, 011603.

(14) Jiang, B.; Qiu, P.; Eikeland, E.; Chen, H.; Song, Q.; Ren, D.; Zhang, T.; Yang, J.; Iversen, B. B.; Shi, X.; et al. Cu_8GeSe_6-Based Thermoelectric Materials with an Argyrodite Structure. *J. Mater. Chem. C* **2017**, *5*, 943−952.

(15) Kuhs, W. F.; Nitsche, R.; Scheunemann, K. The Argyrodites—A New Family of Tetrahedrally Close-Packed Structures. *Mater. Res. Bull.* **1979**, *14*, 241−248.

(16) Shen, X.; Yang, C.-C.; Liu, Y.; Wang, G.; Tan, H.; Tung, Y.-H.; Wang, G.; Lu, X.; He, J.; Zhou, X. High-Temperature Structural and Thermoelectric Study of Argyrodite Ag_8GeSe_6. *ACS Appl. Mater. Interfaces* **2019**, *11*, 2168−2176.

(17) Kharakhorin, F. F.; Petrov, V. M. Semiconducting Properties of Compounds of the $A_2^{I}B^{IV}C_3^{VI}$Type. *Fiz. Tverd. Tela/Akad. Nauk SSSR* **1964**, *6*, 1867−2869.

(18) Balanevskaya, A. E.; Berger, L. I.; Petrov, V. M. Semiconductor and Physical Chemical Properties of a Series of Ternary Compounds of the Type $A_2^{I}B^{IV}C_3^{VI}$. *Izv. Akad. Nauk SSSR, Neorg. Mater.* **1966**, *2*, 810−813.

(19) Astakhov, O. P.; Berger, L. I.; Dovletov, K. Electrical Conductivity and Thermoelectromotive Force of Ternary Semiconductor Alloys with Ag_2GeSe_3 and Ag_2SnSe_3 Composition in Solid and Liquid States. *Izv. Akad. Nauk Turkm. SSR, Ser. Fiz.-Tekh., Khim. Geol. Nauk* **1968**, *3*, 104−105.

(20) Astakhov, O. P.; Berger, L. I.; Dovletov, K. Thermoelectric Properties of Semiconductors of Ag_2GeTe_3 and Ag_2SnTe_3 Alloys in Solid and Liquid States. *Izv. Akad. Nauk Turkm. SSR, Ser. Fiz.-Tekh., Khim. Geol. Nauk* **1968**, *4*, 121−122.

(21) Khanafer, M.; Gorochov, O.; Rivet, J. Electrical Properties of the Phases Copper Thiogermanate (Cu_2GeS_3 and Cu_8GeS_6) and Copper Thiostannate (Cu_2SnS_3 and Cu_4SnS_4). *Mater. Res. Bull.* **1974**, *9*, 1543−1552.

(22) Shi, X.; Xi, L.; Fan, J.; Zhang, W.; Chen, L. Cu-Se Bond Network and Thermoelectric Compounds with Complex Diamond-like Structure. *Chem. Mater.* **2010**, *22*, 6029−6031.

(23) Cho, J. Y.; Shi, X.; Salvador, J. R.; Meisner, G. P.; Yang, J.; Wang, H.; Wereszczak, A. A.; Zhou, X.; Uher, C. Thermoelectric Properties and Investigations of Low Thermal Conductivity in Ga-Doped Cu_2GeSe_3. *Phys. Rev. B: Condens. Matter Mater. Phys.* **2011**, *84*, 085207.

(24) Dugarte-Dugarte, A.; Ramírez Pineda, N.; Nieves, L.; Henao, J. A.; Díaz de Delgado, G.; Delgado, J. M. The Crystal Structure of

Cu_2GeSe_3 and the Structure-Types of the I_2-IV-VI_3 family of Semiconducting Compounds. *Acta Crystallogr., Sect. B: Struct. Sci., Cryst. Eng. Mater.* **2021**, *77*, 158−167.
(25) Shao, H.; Tan, X.; Hu, T.; Liu, G.-Q.; Jiang, J.; Jiang, H. First-Principles Study on the Lattice Dynamics and Thermodynamic Properties of Cu_2GeSe_3. *Epl* **2015**, *109*, 47004.
(26) Nagel, A.; Range, K.-J. Compound Formation in the System Ag_2S-GeS_2-AgI. *Z. Naturforsch.* **1978**, *33*, 1461−1464.
(27) Giannozzi, P.; Baroni, S.; Bonini, N.; Calandra, M.; Car, R.; Cavazzoni, C.; Ceresoli, D.; Chiarotti, G. L.; Cococcioni, M.; Dabo, I.; et al. QUANTUM ESPRESSO: A Modular and Open-Source Software Project for Quantum Simulations of Materials. *J. Phys.: Condens. Matter* **2009**, *21*, 395502.
(28) Perdew, J. P.; Burke, K.; Ernzerhof, M. Generalized Gradient Approximation Made Simple. *Phys. Rev. Lett.* **1996**, *77*, 3865−3868.
(29) Perdew, J. P.; Ruzsinszky, A.; Csonka, G. I.; Vydrov, O. A.; Scuseria, G. E.; Constantin, L. A.; Zhou, X.; Burke, K. Restoring the Density-Gradient Expansion for Exchange in Solids and Surfaces. *Phys. Rev. Lett.* **2008**, *100*, 136406.
(30) Vanderbilt, D. Soft Self-Consistent Pseudopotentials in a Generalized Eigenvalue Formalism. *Phys. Rev. B: Condens. Matter Mater. Phys.* **1990**, *41*, 7892−7895.
(31) Rappe, A. M.; Rabe, K. M.; Kaxiras, E.; Joannopoulos, J. D. Optimized Pseudopotentials. *Phys. Rev. B: Condens. Matter Mater. Phys.* **1990**, *41*, 1227−1230.
(32) Monkhorst, H. J.; Pack, J. D. Special Points for Brillouin-Zone Integrations. *Phys. Rev. B: Solid State* **1976**, *13*, 5188−5192.
(33) Marini, A.; Hogan, C.; Grüning, M.; Varsano, D. Yambo: An Ab Initio Tool for Excited State Calculations. *Comput. Phys. Commun.* **2009**, *180*, 1392−1403.
(34) Sangalli, D.; Ferretti, A.; Miranda, H.; Attaccalite, C.; Marri, I.; Cannuccia, E.; Melo, P.; Marsili, M.; Paleari, F.; Marrazzo, A.; et al. Many-Body Perturbation Theory Calculations Using the Yambo Code. *J. Phys.: Condens. Matter* **2019**, *31*, 325902.
(35) Schlipf, M.; Gygi, F. Optimization Algorithm for the Generation of ONCV Pseudopotentials. *Comput. Phys. Commun.* **2015**, *196*, 36−44.
(36) Bruneval, F.; Gonze, X. Accurate GW Self-Energies in a Plane-Wave Basis Using Only a Few Empty States: Towards Large Systems. *Phys. Rev. B: Condens. Matter Mater. Phys.* **2008**, *78*, 085125.
(37) Togo, A.; Tanaka, I. First Principles Phonon Calculations in Materials Science. *Scr. Mater.* **2015**, *108*, 1−5.
(38) Fan, T.; Oganov, A. R. AICON: A Program for Calculating Thermal Conductivity Quickly and Accurately. *Comput. Phys. Commun.* **2020**, *251*, 107074.
(39) Reshak, A. H.; Auluck, S.; Piasecki, M.; Myronchuk, G. L.; Parasyuk, O.; Kityk, I. V.; Kamarudin, H. Absorption and Photoconductivity Spectra of Ag_2GeS_3 Crystal: Experiment and Theory. *Spectrochim. Acta, Part A* **2012**, *93*, 274−279.
(40) Wang, N. The Ag-Ge-S System: New Experimental Results. *Neues Jahrb. Mineral., Abh.* **1995**, *169*, 313−317.
(41) Armand, P.; Ibanez, A.; Tonnerre, J.-M.; Bouchet-Fabre, B.; Philippot, E. Structural Characterization of Glass by Anomalous Wide-Angle x-Ray Scattering. *Phys. Rev. B: Condens. Matter Mater. Phys.* **1997**, *56*, 10852−10859.
(42) Eulenberger, G. The Crystal Structure of the Low Temperature Form of Synthetic Argyrodite Ag_8GeS_6. *Monatsh. Chem.* **1977**, *108*, 901−913.
(43) Fedorchuk, A. O.; Lakshminarayana, G.; Tokaychuk, Y. O.; Parasyuk, O. V. The Crystal Structure of Novel Silver Sulphogermanate Ag_8GeS_6. *J. Alloys Compd.* **2013**, *576*, 134−139.
(44) Bermann, R. *Thermal Conduction in Solids*; Clarendon Press, 1976.
(45) Xing, T.; Zhu, C.; Song, Q.; Huang, H.; Xiao, J.; Ren, D.; Shi, M.; Qiu, P.; Shi, X.; Xu, F.; et al. Ultralow Lattice Thermal Conductivity and Superhigh Thermoelectric Figure-of-Merit in (Mg, Bi) Co-Doped GeTe. *Adv. Mater.* **2021**, *33*, 2008773.
(46) Koley, B.; Lakshan, A.; Raghuvanshi, P. R.; Singh, C.; Bhattacharya, A.; Jana, P. P. Ultralow Lattice Thermal Conductivity at Room Temperature in Cu_4TiSe_4. *Angew. Chem., Int. Ed.* **2021**, *60*, 9106−9113.
(47) Damay, F.; Petit, S.; Rols, S.; Braendlein, M.; Daou, R.; Elkaïm, E.; Fauth, F.; Gascoin, F.; Martin, C.; Maignan, A. Localised Ag^+ Vibrations at the Origin of Ultralow Thermal Conductivity in Layered Thermoelectric $AgCrSe_2$. *Sci. Rep.* **2016**, *6*, 23415.
(48) Spitzer, D. P. Lattice Thermal Conductivity of Semiconductors: A Chemical Bond Approach. *J. Phys. Chem. Solids* **1970**, *31*, 19−40.
(49) Koley, B.; Lakshan, A.; Raghuvanshi, P. R.; Singh, C.; Bhattacharya, A.; Jana, P. P. Ultralow Lattice Thermal Conductivity at Room Temperature in Cu_4TiSe_4. *Angew. Chem., Int. Ed.* **2021**, *60*, 9106−9113.
(50) Roychowdhury, S.; Ghosh, T.; Arora, R.; Samanta, M.; Xie, L.; Singh, N. K.; Soni, A.; He, J.; Waghmare, U. V.; Biswas, K. Enhanced Atomic Ordering Leads to High Thermoelectric Performance in $AgSbTe_2$. *Science* **2021**, *371*, 722−727.
(51) Lin, H.; Tan, G.; Shen, J. N.; Hao, S.; Wu, L. M.; Calta, N.; Malliakas, C.; Wang, S.; Uher, C.; Wolverton, C.; et al. Concerted Rattling in $CsAg_5Te_3$ Leading to Ultralow Thermal Conductivity and High Thermoelectric Performance. *Angew. Chem., Int. Ed.* **2016**, *55*, 11431−11436.
(52) Kurosaki, K.; Kosuga, A.; Muta, H.; Uno, M.; Yamanaka, S. Ag_9TlTe_5: A High-Performance Thermoelectric Bulk Material with Extremely Low Thermal Conductivity. *Appl. Phys. Lett.* **2005**, *87*, 061919.
(53) Mukhopadhyay, S.; Parker, D. S.; Sales, B. C.; Puretzky, A. A.; McGuire, M. A.; Lindsay, L. Two-Channel Model for Ultralow Thermal Conductivity of Crystalline Tl_3VSe_4. *Science* **2018**, *360*, 1455−1458.
(54) Jana, M. K.; Pal, K.; Waghmare, U. V.; Biswas, K. The Origin of Ultralow Thermal Conductivity in InTe: Lone-Pair-Induced Anharmonic Rattling. *Angew. Chem., Int. Ed.* **2016**, *55*, 7792−7796.
(55) Zhao, L.-D.; Lo, S.-H.; Zhang, Y.; Sun, H.; Tan, G.; Uher, C.; Wolverton, C.; Dravid, V. P.; Kanatzidis, M. G. Ultralow Thermal Conductivity and High Thermoelectric Figure of Merit in SnSe Crystals. *Nature* **2014**, *508*, 373−377.
(56) Qiu, W.; Xi, L.; Wei, P.; Ke, X.; Yang, J.; Zhang, W. Part-Crystalline Part-Liquid State and Rattling-like Thermal Damping in Materials with Chemical-Bond Hierarchy. *Proc. Natl. Acad. Sci. U.S.A.* **2014**, *111*, 15031−15035.
(57) Liu, H.; Shi, X.; Xu, F.; Zhang, L.; Zhang, W.; Chen, L.; Li, Q.; Uher, C.; Day, T.; Snyder, G. J. Copper Ion Liquid-like Thermoelectrics. *Nat. Mater.* **2012**, *11*, 422−425.
(58) Brown, S. R.; Kauzlarich, S. M.; Gascoin, F.; Snyder, G. J. $Yb_{14}MnSb_{11}$: New High Efficiency Thermoelectric Material for Power Generation. *Chem. Mater.* **2006**, *18*, 1873−1877.
(59) Kubelka, P.; Munk, F. An Article on Optics of Paint Layers. *Z. Tech. Phys.* **1931**, *12*, 593−601.
(60) Tauc, J.; Grigorovici, R.; Vancu, A. Optical Properties and Electronic Structure of Amorphous Germanium. *Phys. Status Solidi B* **1966**, *15*, 627−637.
(61) Mukhopadhyay, S.; Singh, D. J.; Reinecke, T. L. Ultralow Thermal Conductivity in Cs-Sb-Se Compounds: Lattice Instability versus Lone-Pair Electrons. *Chem. Mater.* **2020**, *32*, 8906−8913.
(62) Xie, L.; Feng, J. H.; Li, R.; He, J. Q. First-Principles Study of Anharmonic Lattice Dynamics in Low Thermal Conductivity $AgCrSe_2$: Evidence for a Large Resonant Four-Phonon Scattering. *Phys. Rev. Lett.* **2020**, *125*, 245901.
(63) Xia, Y.; Ozoliņš, V.; Wolverton, C. Microscopic Mechanisms of Glasslike Lattice Thermal Transport in Cubic $Cu_{12}Sb_4S_{13}$ Tetrahedrites. *Phys. Rev. Lett.* **2020**, *125*, 085901.
(64) Pöhls, J.-H.; Chanakian, S.; Park, J.; Ganose, A. M.; Dunn, A.; Friesen, N.; Bhattacharya, A.; Hogan, B.; Bux, S.; Jain, A.; et al. Experimental Validation of High Thermoelectric Performance in $RECuZnP_2$ predicted by High-Throughput DFT Calculations. *Mater. Horiz.* **2021**, *8*, 209−215.
(65) Zhu, Y.; Wei, B.; Liu, J.; Koocher, N. Z.; Li, Y.; Hu, L.; He, W.; Deng, G.; Xu, W.; Wang, X.; et al. Physical Insights on the Low

https://doi.org/10.1021/acs.chemmater.2c01050
Chem. Mater. 2022, 34, 6420−6430

Lattice Thermal Conductivity of $AgInSe_2$. *Mater. Today Phys.* **2021**, *19*, 100428.
(66) Zhang, Y. First-Principles Debye−Callaway Approach to Lattice Thermal Conductivity. *J. Materiomics* **2016**, *2*, 237−247.
(67) Chan, M. K. Y.; Ceder, G. Efficient Band Gap Prediction for Solids. *Phys. Rev. Lett.* **2010**, *105*, 196403.
(68) Pal, K.; Park, C. W.; Xia, Y.; Shen, J.; Wolverton, C. Scale-Invariant Machine-Learning Model Accelerates the Discovery of Quaternary Chalcogenides with Ultralow Lattice Thermal Conductivity. *npj Comput. Mater.* **2022**, *8*, 48.
(69) Schelling, P. K.; Phillpot, S. R.; Keblinski, P. Comparison of Atomic-Level Simulation Methods for Computing Thermal Conductivity. *Phys. Rev. B: Condens. Matter Mater. Phys.* **2002**, *65*, 144306.
(70) McGaughey, A. J. H.; Kaviany, M. Phonon Transport in Molecular Dynamics Simulations: Formulation and Thermal Conductivity Prediction. *Adv. Heat Transfer* **2006**, *39*, 169−255.
(71) McQuarrie, D. A. *Statistical Mechanics*; Woods, John, A., Eds.; Harper & Row: New York, 1976.

https://doi.org/10.1021/acs.chemmater.2c01050
Chem. Mater. 2022, 34, 6420−6430